Nanoscale

Tuning epitaxial growth on NaYbF4 upconversion nanoparticles by strain management

Journal:	*Nanoscale*
Manuscript ID	NR-ART-04-2020-003374.R1
Article Type:	Paper
Date Submitted by the Author:	31-May-2020

Complete List of Authors:	Zhao, Jianxiong; City University of Hong Kong, Department of Materials Science and Engineering Chen, Bing; City University of Hong Kong College of Science and Engineering, Department of Materials Science and Engineering CHEN, Xian; Shenzhen University, College of Materials Science and Engineering Zhang, Xin; City University of Hong Kong, Department of Materials Science and Engineering Sun, Tianying; City University of Hong Kong, Department of Materials Science and Engineering Su, Dong ; Chinese Academy of Sciences Institute of Physics Wang, Feng; City University of Hong Kong, Department of Materials Science and Engineering

PAPER

Tuning Epitaxial Growth on $NaYbF_4$ Upconversion Nanoparticles by Strain Management

Received 00th January 20xx,
Accepted 00th January 20xx

DOI: 10.1039/x0xx00000x

Jianxiong Zhao[ad], Bing Chen[ad], Xian Chen[b], Xin Zhang[ad], Tianying Sun[ad], Dong Su[c], and Feng Wang[ad]*

Core–shell structural engineering is a common strategy for tuning upconversion luminescence in lanthanide-doped nanoparticles. However, epitaxial growth on hexagonal phase $NaYbF_4$ nanoparticles typically suffers from incomplete shell coverage due to the large and anisotropic interfacial strain. Herein, we explore the effects of core particle size and morphology as well as reaction temperature on controlling the epitaxial growth of $NaGdF_4$ shells on $NaYbF_4$ nanoparticles with misfit parameters of f_a = 1.58% and f_l = 2.24% for axial and lateral growth, respectively. Rod-like core particles with a long length and a large diameter are found to promote shell growth with high surface coverage by facilitating the relaxation of lattice strains. Furthermore, the primary $NaGdF_4$ shell can serve as a transition layer to mediate the growth of additional $NaNdF_4$ coating layers that display an even larger lattice misfit with the core (f_a = 2.98%; f_l = 4.32%). The resultant $NaYbF_4$@Na(Gd/Nd)F_4 core–shell nanostructures simultaneously show strong multiphoton upconversion luminescence and superior magnetic resonance T_1 ionic relaxivity. Our findings are important for the rational design of core–shell upconversion nanoparticles with optimized property and functionality for technological applications.

Introduction

Core–shell structure has become an indispensable configuration for constructing advanced upconversion nanoparticles. By protecting a doped core nanoparticle (e.g.; $NaYF_4$:Yb/Er) with an inert shell (e.g.; $NaYF_4$), the surface quenching processes can be effectively eliminated, leading to a large enhancement of radiative emission and alleviation of concentration quenching.[1-11] The spectral tunability of upconversion emissions can also be greatly expanded by incorporating a set of lanthanide ions into separate layers of a core–shell nanoparticle.[12-17] For example, by leveraging energy migration in core–shell structured nanoparticles, highly designable upconversion processes have been realized in a wide collection of activator ions including Tb^{3+}, Eu^{3+}, Dy^{3+}, Sm^{3+}, Mn^{2+}, Nd^{3+}, and Ce^{3+} by multiwavelength excitation across 800 to 1550 nm.[18-25] These core–shell upconversion nanoparticles displaying unprecedented optical emissions have unlocked technological applications in diverse fields encompassing biology, energy, and photonics.[26-34]

Despite the remarkable capability for tuning upconversion, the preparations of core–shell nanoparticles of arbitrary core/shell combinations have not yet been fully addressed. As heteroepitaxy processes are influences by interfacial strains between the core and shell layers, epitaxial deposition of the shell layer on core particles may be hindered under large lattice misfit.[9,35-38] For instance, a misfit parameter of over 1.5% in the epitaxial coating of β-$NaYF_4$:Yb/Er nanoparticles can result in a strong facet-dependence of interfacial strains, leading to highly unbalanced epitaxy in different crystallographic directions.[15,36] On account of the anisotropic interfacial strain, very limited success has been achieved in the epitaxial coating of $NaYbF_4$ upconversion nanoparticles, which has been identified as one of the most efficient host materials for multiphoton upconversion.[39-43] Due to the substantially small lattice constant of $NaYbF_4$ in the $NaLnF_4$ (Ln = lanthanide) series, only a limited number of well-selected shell layers such as $NaLuF_4$ and $NaYF_4$ have been successfully grown on $NaYbF_4$ nanoparticles to date.[29,38] The growth of light and medium lanthanide-based shells on $NaYbF_4$ for tuning the properties of the core nanoparticles remains a daunting challenge. Light and medium lanthanides such as Gd^{3+}, Dy^{3+}, and Nd^{3+} are important shell components that tune the magnetic resonance ionic relaxivity and excitation property of upconversion nanoparticles for various biomedical applications.[44,45]

In this work, we describe an experimental investigation of epitaxial growth on β-$NaYbF_4$ nanoparticles under large anisotropic interfacial strain. We demonstrate rational control of the epitaxial habits by tuning the dimension of $NaYbF_4$ core nanoparticles and reaction temperature. Under optimized conditions, mismatched $NaGdF_4$ and $NaNdF_4$ shells are grown on $NaYbF_4$ core nanoparticles with high surface coverage. Based on the core/shell combinations, high magnetic resonance T_1

[a] Department of Materials Science and Engineering, City University of Hong Kong, 83 Tat Chee Avenue, Hong Kong SAR, China. E-mail: fwang24@cityu.edu.hk
[b] College of Materials Science and Engineering, Shenzhen University, Shenzhen 518060, China
[c] Beijing National Laboratory for Condensed Matter Physics, Institute of Physics, Chinese Academy of Sciences, Beijing, 100190, China
[d] City University of Hong Kong Shenzhen Research Institute, Shenzhen 518057, China
† Footnotes relating to the title and/or authors should appear here.
Electronic Supplementary Information (ESI) available: [details of any supplementary information available should be included here]. See DOI: 10.1039/x0xx00000x

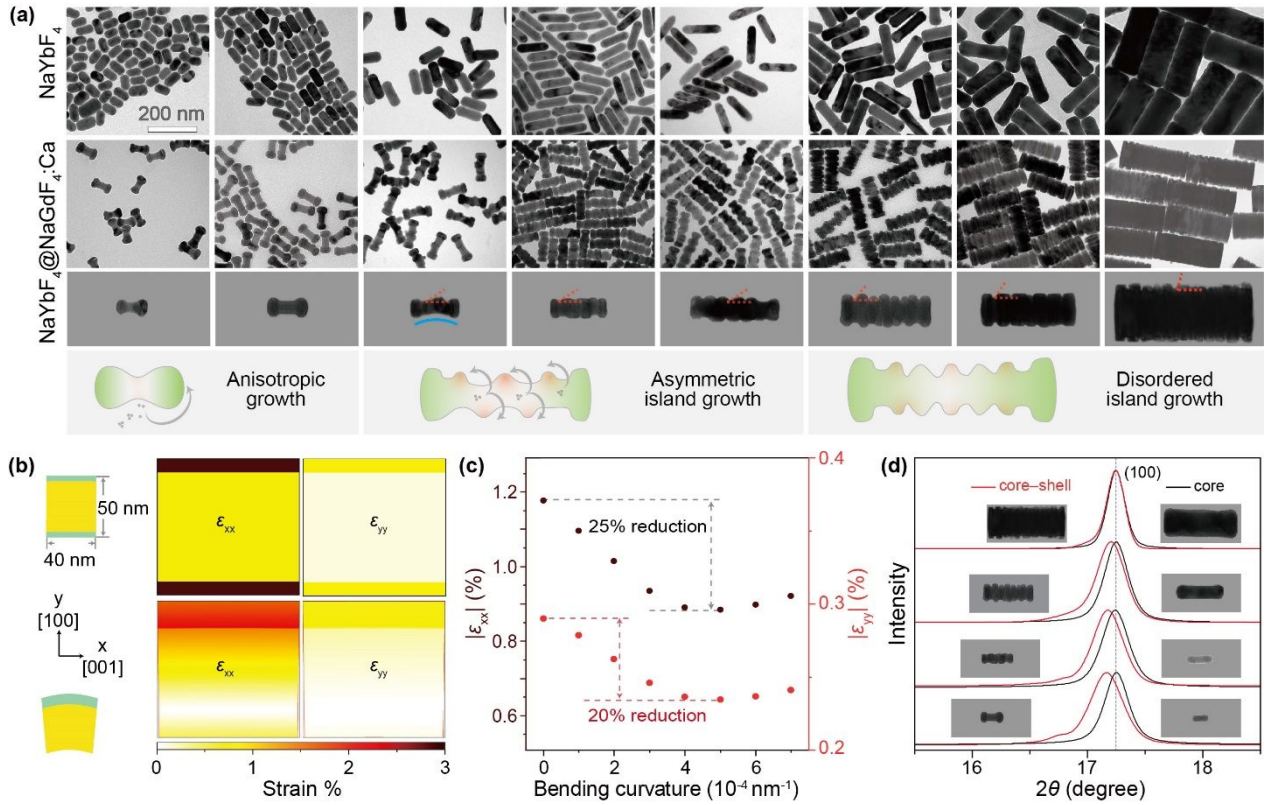

Fig. 1 (a) TEM images of $NaYbF_4$ core nanorods with different sizes and the resultant $NaYbF_4$@$NaGdF_4$:Ca (30%) core–shell nanorods. The contact angle is estimated in the magnified TEM images. (b) Calculated strain distribution in the core–shell structures with symmetric (top panel) and asymmetric (bottom panel; bending curvature: 5×10^{-4} nm^{-1}) shell configurations, respectively. (c) Calculated mean strains as a function of the bending curvature for the model in (b). (d) Core particle size-dependent strain relaxation revealed by the shift of major (100) peak.

ionic relaxivity and strong deep UV emissions are simultaneously achieved.

Results and discussion

The lattice constant of $NaYbF_4$ is the second smallest among the $NaLnF_4$ series. Epitaxial deposition of $NaGdF_4$ on prism facets of hexagonal phase $NaYbF_4$ nanoparticles is relatively slow and the prism shells may eventually be decomposed (**Fig. S1**) due to larger lattice misfit for the epitaxial growth in the lateral (f_l = 2.51%) than the axial (f_a = 1.82%) directions (**Fig. S2** and **Table S1** and **S2**).[36] We reason that effective epitaxy on the prism facets could be achieved if the misfit strain in the prism shells is effectively relaxed without introducing significant lattice defects.

To validate our hypothesis, $NaYbF_4$ nanorods of varying sizes were synthesized and used for epitaxial growth of $NaGdF_4$ shells by rational control of the heating rate and the oleic acid (OA)/oleylamine (OM) ratio in the solvent (**Fig. S3**).[46] The rod-shaped core nanoparticles were designed to offer structural flexibility for a partial relaxation of the strain by mechanical bending.[47-50] The nanorod core particles also provided a large prism facet to permit the Stranski-Krastanov epitaxy mode, which is characterized by an island-like growth pattern essential for relaxing lattice strains.[51,52] Besides, Ca^{2+} dopants were introduced to the shell to increase the growth affinity and to facilitate the release of strain energy through local lattice bending.[36]

Fig. 1 shows the TEM image of different $NaYbF_4$ core nanoparticles and the corresponding $NaYbF_4$@$NaGdF_4$:Ca (30%) core–shell nanoparticles synthesized by a consistent heat-up protocol.[53] The dopant concentration of Ca^{2+} was optimized to minimize the self-nucleation of shell precursors (**Fig. S4**). XRD patterns confirmed the pure hexagonal phase of all the core and core–shell nanoparticles (**Fig. S5**). As anticipated, the shell coverage on the prism facets was significantly improved with increasing length and diameter of the core nanorods (**Fig. 1a** and **Fig. S6**). In general, the prism shells adopted island-like morphologies in agreement with the Stranski-Krastanov growth mode, which effectively released the strain energy in comparison with the uniform and conformal shells.[54] The island-like shell featured preferential growth in the [100] directions due to the relatively small lattice misfit, giving rise to a ribbed structure (**Fig. S7**).

The evolution of the shell morphology as the size and shape of the core nanorods changed was ascribed to a variation in the strain reduction/relaxation mechanism. Three types of epitaxy patterns can be identified (**Fig. 1a**, bottom panel). For core

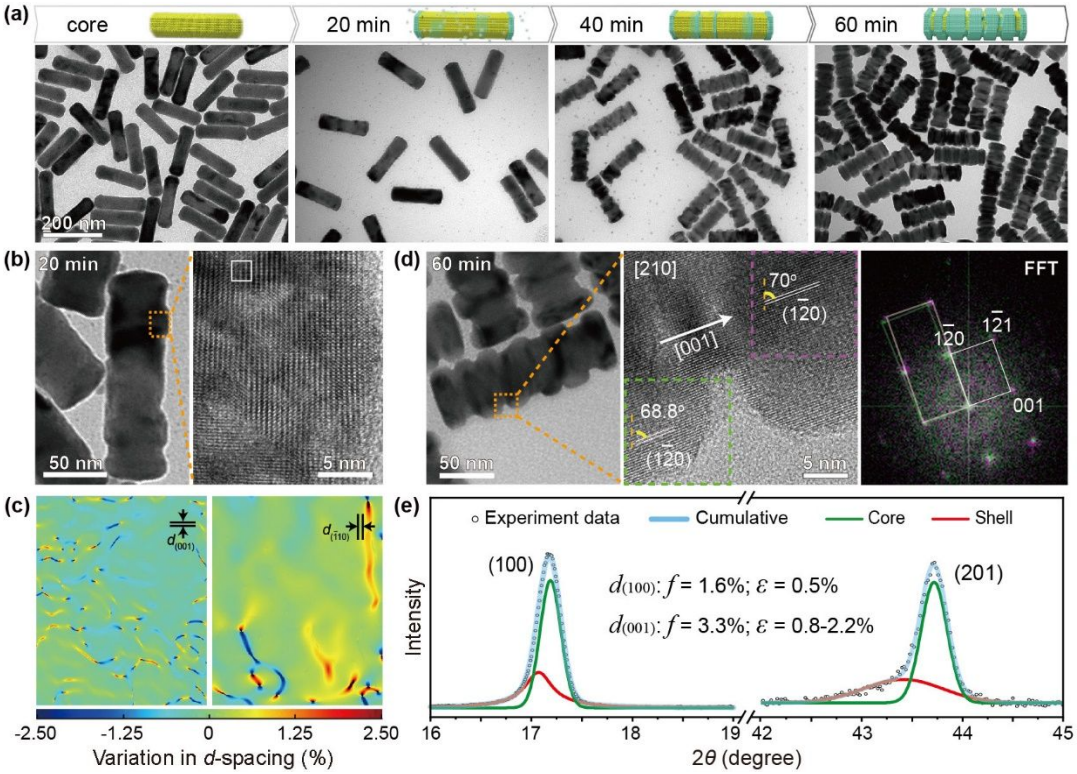

Fig. 2 (a) TEM images of the $NaYbF_4$@$NaGdF_4$:Ca (30%) core–shell structure at different stages of the synthesis. (b) Low-magnification and high-resolution TEM images of the $NaYbF_4$@$NaGdF_4$:Ca (30%) nanorods extracted at the early stage (20 min) of the epitaxy. (c) GPA analysis of the high-resolution TEM image in (b). A small area at the upper left corner (indicated by square) was used as the reference. (d) Low-magnification and high-resolution TEM images of the $NaYbF_4$@$NaGdF_4$:Ca (30%) nanorods extracted at the late stage (60 min) of the epitaxy and the joint diffractogram obtained by overlapping the FFT patterns for the core and shell domains (indicated by magenta and green squares). (e) XRD patterns of the $NaYbF_4$@$NaGdF_4$:Ca (30%) core–shell structure with single peak deconvolution. The calculated misfit strain for the island layer was smaller than the misfit parameter, supporting partial relaxation of misfit strain.

particles of short nanorods, dumbbell-shaped core–shell nanoparticles were formed with shell layers dominantly deposited on basal facets of the core nanorods. The results were ascribed to the decomposition of the strained prism layers at the late stage of the epitaxy (**Fig. S8**), in resemblance to the process previously observed for epitaxial coating of $NaNdF_4$ shell on spherical $NaYF_4$: Yb/Er core nanoparticles.[36]

As the length of the nanorods increased, the critical normal stress (σ_{CR}) to induce bending of the nanorod decreased as described by equation 1.[55,56-58]

$$\sigma_{CR} = \frac{\pi^2 E}{\left(\frac{L}{R}\right)^2} \qquad (1)$$

where *E*, *R*, and *L* are Young's modulus, radius, and length of the nanorod, respectively. As a result, misfit strain was readily relaxed by bending of the core nanorods in association with island shells formed on the prism facet with an anticorrelated configuration, which exerted asymmetric stress on the core. Our theoretical calculating confirmed the appreciable decease of lattice strains in both core and shell layers by a slight bending of the core nanorods (**Fig. 1b** and **c**, **Fig. S9**).

With further increase in the diameter of the long nanorods, the core nanorods ceased to bend due to the increased critical normal stress. Nevertheless, the surface area of prism facets became sufficiently large to allow extensive Stranski-Krastanov mode of growth by providing multiple sites for heterogeneous nucleation.[51] Under this growth mode, disordered island shells were formed on the prism facet to minimize the lattice strains. Our XRD analyses (**Fig. 1d** and **Fig. S10**) supported the continuous relaxation of misfit strain with the increase of the core particle size by detecting a steady reduction of lattice strain in the core layer. The reduction of average lattice strain was also partly ascribed to the decreased interaction between the core and shell layers, as indicated by the increase in the contact angle of the epitaxial shell on the core nanorods. A high contact angle led to a reduced interfacial area and thus a decreased overall strain energy.[54]

To shed more light on the strain relaxation process in the shell layers, TEM images of the $NaGdF_4$ shells deposited on the thick $NaYbF_4$ nanorods (180 × 45 nm) were recorded at various stages of the synthesis. The results shown in **Fig. 2a** revealed an evolution of shell morphology from uniform thin sheets to irregular islands as the epitaxial growth proceeded, which was

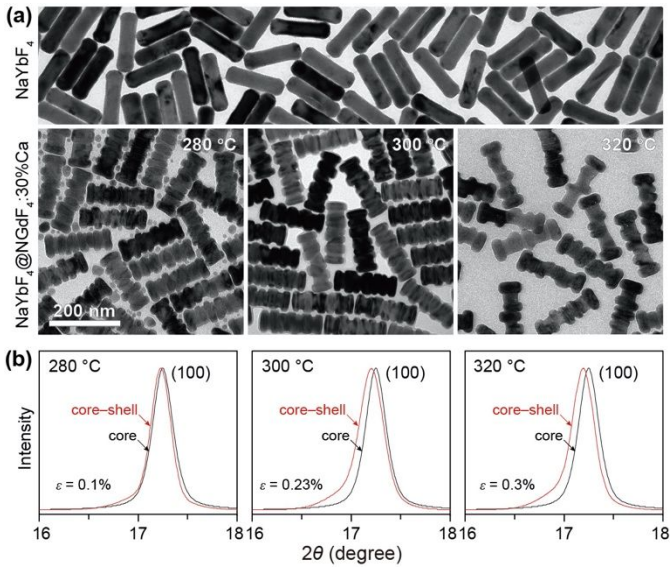

Fig. 3 (a) TEM images of the core $NaYbF_4$ nanoparticles and corresponding $NaYbF_4$@$NaGdF_4$:Ca (30%) core–shell nanoparticles with the shell layers deposited at different temperatures. (b) (100) peak from XRD patterns of the core and core–shell nanoparticles in (a). The lattice strain (ε) was calculated based on the difference in the (100) *d*-spacing before and after shell deposition.

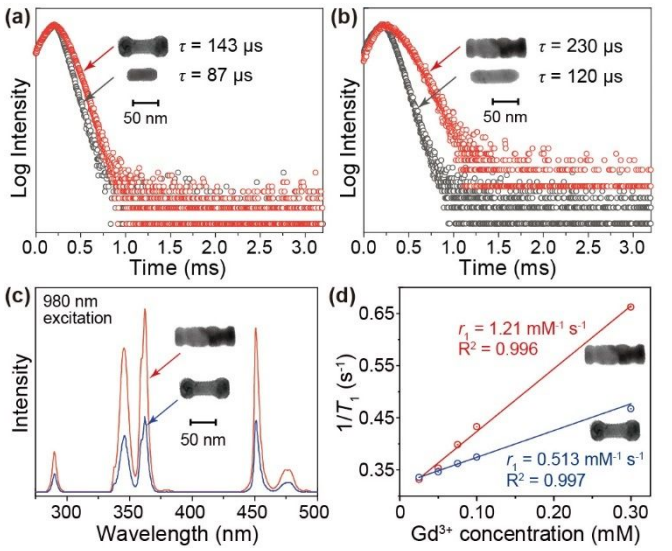

Fig. 4 Comparison of time decay of Tm^{3+} emission at 290 nm in (a) dumbbell-like and (b) ribbed $NaYbF_4$:Tm (1%)@$NaGdF_4$:Ca (30%) core–shell nanorods and their corresponding core nanorods. (c) Emission spectra of the ribbed and dumbbell-like $NaYbF_4$:Tm (1%)@$NaGdF_4$:Ca (30%) core–shell nanorods under excitation of 980 nm. (d) The T_1 ionic relaxivity plots against the Gd^{3+} concentration for the ribbed and dumbbell-like nanostructures at a magnetic field of 3T. The slope indicates the corresponding specific ionic relaxivity (r_1).

in accord with the Stranski-Krastanov growth mode. According to high-resolution TEM and corresponding geometric phase analysis (GPA), the thin sheet shells were homogeneously strained by meshing to the core lattice (**Fig. 2b** and **c**). Due to positive Poisson's ratio, the shell layer was homogeneously contracted along (001) direction and expanded along (110) directions.[36]

As the shell thickness increased, island shells were developed for relaxation of the strain energy. The island shells were only partly strained by forming shear deformations relative to the core lattice. High-resolution TEM image that was taken along the [210] zone axis of a $NaYbF_4$@$NaGdF_4$:Ca (30%) nanorod showed an obvious tilt of the (120) plane in both real and reciprocal space (**Fig. 2d**). XRD peak analysis confirmed that the misfit strain (ε) in both the (100) and (001) crystallographic directions were smaller than the corresponding misfit parameter (f) (**Fig. 2e**), supporting partial relaxation of the misfit strain in the shell layer. It is worth noting that the Stranski-Krastanov growth typically occurs under large lattice misfits of over 5% that result in small activation energy.[59,60] The 3D island growth observed here was ascribed to the rough surface originating from the inherent instability of the strained shell (Fig. 2b), which lowers the energy barrier for island formation.[61]

The epitaxial growth mechanism and shell morphology were found to be affected by the reaction temperature as well (**Fig. 3a**). For a typical shell growth at 300 °C, the island morphology was due to the Stranski-Krastanov growth mode. At an elevated temperature (320 °C), atom diffusion was enhanced as a result of the decreased energy barriers. Accordingly, the shell was transformed into fewer and larger islands.[54] Besides, the critical normal stress (σ_{CR}) of the core particle also decreased at high temperature due to the reduction of Young's modulus, resulting in bending of the core nanorods.[62] As the reaction temperature dropped to 280 °C, the growth affinity of the shell layers on core nanorods was reduced, resulting in the formation of secondary small nanoparticles by self-nucleation of shell precursors.[36] XRD analyses revealed an increase in misfit strain as the reaction temperature was elevated (**Fig. 3b**), in agreement with the TEM observations.

The success in rational control of $NaGdF_4$ epitaxy on $NaYbF_4$ core nanorods offers great opportunities for designing advanced upconversion nanomaterials.[63] In comparison with the dumbbell-shaped counterparts, the ribbed $NaYbF_4$:Tm (1%)@$NaGdF_4$ core–shell nanoparticles featuring a high shell coverage were more effectively protected against surface quenching (**Fig. 4a**,**b**), leading to intense multiphoton upconversion emission from the Tm^{3+} activators after near-infrared (NIR) excitation at 980 nm (**Fig. 4c**). The high surface coverage of the $NaGdF_4$ also contributed to the effective relaxation of water molecules in an aqueous solution for magnetic resonance imaging (MRI; **Fig. 4d**). Partly owing to the island nature of the shell layer, the nanoparticles extensively interacted with the surrounding water molecules, giving rise to a high T_1 ionic relaxivity of 1.21 mM^{-1} s^{-1}, comparable to that offered by small nanoparticles (**Fig. S11**).

As an added benefit, the $NaGdF_4$ shell can act as a transition layer to mediate the growth of $NaNdF_4$ shells featuring even larger lattice misfits (f_l = 4.32%; f_a = 2.98%) with the $NaYbF_4$:Tm

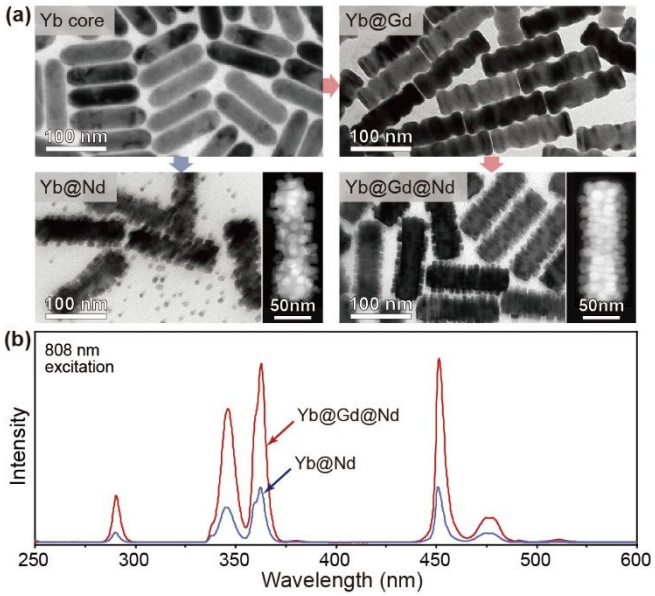

Fig. 5 (a) TEM images of the $NaNdF_4$:Yb (10%) shells grown on the $NaYbF_4$:Tm (1%) nanoparticles without and with the use of a $NaGdF_4$:Ca (30%) transition layer. (b) Emission spectra of the resultant nanoparticles under excitation of 808 nm.

(1%) core nanoparticles (**Fig. 5** and **Fig. S12a**). The formation of the dense $NaNdF_4$:Yb (10%) shells was confirmed by scanning transmission electron microscopy (STEM) (**Fig. 5a**). Through the growth of an Nd-based shell, the multiphoton upconversion emission was achieved by excitation in an expanded range of wavelengths such as 808 nm (**Fig. 5b** and **Fig. S12b**).[64] The introduction of Yb^{3+} dopants in the $NaNdF_4$ shell promoted the energy transfer from the Nd^{3+} sensitizers to the Tm^{3+} activators that resulted in intense UV emission at 290 nm (**Fig. S12c** and **d**). It was noted that the direct growth of $NaNdF_4$ shells on the $NaYbF_4$ particles yielded poor surface coverage and partial decomposition of the core particle due to the substantially large lattice mismatch (**Fig. 5a**), which resulted in the reduction of the upconversion performance (**Fig. 5b**).

Conclusions

In conclusion, this study demonstrates a strategy for rational control of epitaxial growth under large anisotropic interfacial strain by leveraging the shape and size effects of the core nanoparticles. A rod-like core nanoparticle with a long length and large diameter is shown to facilitate strain relaxation by permitting lattice bending and tilting, thereby promoting the epitaxy process. Accordingly, $NaGdF_4$:Ca shell layers of a large lattice mismatch (f_a = 1.58% and f_l = 2.24%) is grown on $NaYbF_4$ nanorods with high surface coverage under an optimal reaction temperature of 300 °C. The $NaGdF_4$ shells can mediate further epitaxial growth of $NaNdF_4$ shells featuring an even large lattice misfit with the core (f_a = 2.98%; f_l = 4.32%). These novel core–shell nanostructures simultaneously provide high magnetic resonance T_1 ionic relaxivity and strong multiphoton upconversion emission by multiwavelength NIR excitation. Our methods can be readily extended to synthesize other types of core–shell nanoparticles featuring a large difference in core/shell compositions, thereby enhancing our abilities to control the property and functionality of nanostructured materials.

Experimental section

Chemicals. Lanthanide acetate hydrate (99.9%), calcium acetate hydrate (C1000, 99%), ammonium fluoride (216011, 98%), 1-octadecene (ODE, O806, 90%), oleic acid (OA, 364525, 90%), oleylamine (OM, O7805, 70%), and polyethylenimine (PEI; branched, MW ≈ 800), were purchased from Sigma-Aldrich. Sodium trifluoroacetate (97%) and sodium hydroxide (98.5%) were purchased from ACROS Organics. Absolute ethyl alcohol (99.85%), methanol (99.99%), and cyclohexane (99.9%) were purchased from VWR International. All chemicals were used as received without further purification.

Synthesis of $NaYbF_4$ core nanorods. The synthesis was adapted from ref. 53. Typically, $Yb(CH_3CO_2)_3$ aqueous solution (0.2 M, 4 mL) was used as the lanthanide precursor, along with 10 mL of OA/OM, and 10 mL of ODE as the solvent. The OA/OM volume ratio was varied to control the nanoparticle size and morphology. Sodium trifluoroacetate (3.2 mmol) in 10 mL methanol solution was used as the sources of sodium and fluoride. The reaction temperature was set at 340 °C with designated heating rates and kept for 1 hr to promote the formation of pure hexagonal phase $NaYbF_4$ (**Figure S3d**).

General procedure for growing $NaGdF_4$ and $NaNdF_4$ shells around core nanoparticles. A mixture of gadolinium/calcium acetate hydrate aqueous solution (0.2 M, 1 mL), 8 mL of OA, and 12 mL of ODE were pipetted into a two-neck round-bottom flask (50 mL) and heated at 160 °C for 1 hr following the method of ref. 36. After cooling down, 4 mL of cyclohexane dispersion of core nanoparticles were added together with a methanol solution (3 mL) containing NH_4F (0.75 mmol) and NaOH (0.5 mmol), followed by stirring for 6 hr at 45 °C. Unless otherwise specified, the mixture was heated at 300 °C for 1 hr under argon atmosphere. To assess the intermediate products, 1 mL of reaction media was extracted every 20 min for TEM observation. The resulting nanoparticles were precipitated, washed, and re-dispersed in 4 mL of cyclohexane. The growth of $NaNdF_4$ and $NaNdF_4$:Yb(10%) shells followed the same protocol, except that neodymium/ytterbium acetate hydrate aqueous solution (0.2 M, 1 mL) were used as the precursors.

Sample characterizations. Low-magnification transmission electron microscopy (TEM) images were taken on an FEI/Philips Tecnai 12 TEM at an acceleration voltage of 120 kV. High-angle annular dark-field scanning transmission electron microscopy (HAADF-STEM) images were obtained on an FEI Titan³ G2 Themis operating at an acceleration voltage of 300 kV. High-resolution TEM images were measured with an FEI Tecnai G2 F30 at 300 kV and a JEOL 2100F TEM at 200kV. The luminescence spectra and time decay curves were recorded with an Edinburgh FLSP980 spectrometer. Powder X-ray diffraction (XRD) patterns were recorded on a Rigaku SmartLab

diffractometer operating at 45 kV and 150 mA at a scanning rate of 2° min^{-1} in the 2θ range from 10° to 80° (Cu Kα radiation, λ = 1.5406 Å). The samples for XRD measurements were prepared by drop-casting 100 μL of nanoparticles onto a fused quartz substrate. The sample alignment was conducted for each measurement. PEI coated nanoparticles for MRI tests were prepared according to the method of ref. 65. The Gd concentrations were calibrated by ICP-OES on an Optima 8000 spectrometer (PerkinElmer). T_1 ionic relaxation measurement was obtained using 3T MAGNETOM Prisma (Siemens Healthcare, Erlangen, Germany). T_1 mapping was determined by spin echo-inversion recovery sequence with inversion times of 200, 400, 600, 800, 1000, 1500, 2000, 3000, 4000, 5000, and 6000 ms and a repetition time of 8000 ms.

Data analysis. The whole pattern XRD fitting was performed by using the Pawley method in the TOPAS 4.2 software.[66] The initial lattice parameters and structure information used for the fitting were derived from ref. 36 (**Table S1**). To probe the strain distribution across the core–shell interface, *d*-spacing maps were calculated by using the STEM_CELL program based on the geometric phase analysis (GPA) algorithm.[67,68] The variation in the (001) and $(\bar{1}10)$ interplanar *d*-spacing was displayed using the false-color maps. To calculate the *d*-spacing from the XRD pattern, the single peak fitting with the Pseudo-Voigt function was applied.[69]

Conflicts of interest

There are no conflicts to declare.

Acknowledgements

The authors acknowledge the assistance on HAADF-STEM observation received from the Electron Microscope Center of Shenzhen University. This work was supported by the National Natural Science Foundation of China (Nos. 21773200 and 21573185), the Research Grants Council of Hong Kong (CityU 11204717 and 11205219), and City University of Hong Kong (7005076). Part of TEM analysis is supported by the Center for Functional Nanomaterials, which is a US DOE Office of Science Facility, at Brookhaven National Laboratory under Contract No. DE-SC0012704.

References

1 B. Liu, C. Li, P. Yang, Z. Hou and J. Lin, *Adv. Mater.*, 2017, **29**, 1605434.
2 Y. Wang, *Nanoscale*, 2019, **11**, 10852.
3 S. Fischer, N. D. Bronstein, J. K. Swabeck, E. M. Chan and A. P. Alivisatos, *Nano Lett.*, 2016, **16**, 7241.
4 T. Sun, R. Ma, X. Qiao, X. Fan and F. Wang, *ChemPhysChem*, 2016, **17**, 766.
5 M. Tang, X. Zhu, Y. Zhang, Z. Zhang, Z. Zhang, Q. Mei, J. Zhang, M. Wu, J. Liu and Y. Zhang, *ACS Nano*, **2019**, **13**, 10405.
6 Z. Wang and A. Meijerink, *J. Phys. Chem. C*, 2018, **122**, 26298.
7 X. Zhu, J. Li, X. Qiu, Y. Liu, W. Feng and F. Li, *Nat. Commun.*, 2018, **9**, 2176.
8 F. T. Rabouw, P. T. Prins, P. Villanueva-Delgado, M. Castelijns, R. G. Geitenbeek and A. Meijerink, *ACS Nano*, 2018, **12**, 4812.
9 D. Hudry, I. A. Howard, R. Popescu, D. Gerthsen and B. S. Richards, *Adv. Mater.*, 2019, **31**, 1900623.
10 X. Chen, D. Peng, Q. Ju and F. Wang, *Chem. Soc. Rev.*, 2015, **44**, 1318.
11 B. Chen and F. Wang, *Acc. Chem. Res.*, **2020**, 53, 358.
12 H. Wen, H. Zhu, X. Chen, T. F. Hung, B. Wang, G. Zhu, S. F. Yu and F. Wang, *Angew Chem. Int. Ed.*, 2013, **52**, 13419.
13 B. Voß, J. Nordmann, A. Uhl, R. Komban and M. Haase, *Nanoscale*, 2013, **5**, 806.
14 L. Schneider, T. Rinkel, B. Voß, A. Chrobak, J. P. Klare, J. Neethling, J. Olivier, D. Schaniel, E.-E. Bendeif and F. Bondino, *Nanoscale*, 2016, **8**, 2832.
15 C. Arboleda, S. He, A. Stubelius, N. J. J. Johnson and A. Almutairi, *Chem. Mater.*, 2019, **31**, 3103.
16 W. Wei, G. Chen, A. Baev, G. S. He, W. Shao, J. Damasco and P. N. Prasad, *J. Am. Chem. Soc.*, 2016, **138**, 15130.
17 G. Tessitore, S. L. Maurizio, T. Sabri and J. A. Capobianco, *Angew Chem. Int. Ed.*, 2019, **58**, 9742.
18 T. Sun, Y. Li, W. L. Ho, Q. Zhu, X. Chen, L. Jin, H. Zhu, B. Huang, J. Lin, B. E. Little, S. T. Chu and F. Wang, *Nat. Commun.*, 2019, **10**, 1811.
19 P. Wang, C. Wang, L. Lu, X. Li, W. Wang, M. Zhao, L. Hu, A. M. El-Toni, Q. Li and F. Zhang, *Biomaterials*, 2017, **141**, 223.
20 Y. Zhong, G. Tian, Z. Gu, Y. Yang, L. Gu, Y. Zhao, Y. Ma and J. Yao, *Adv. Mater.*, 2014, **26**, 2831.
21 F. Wang, R. Deng, J. Wang, Q. Wang, Y. Han, H. Zhu, X. Chen and X. Liu, *Nat. Mater.*, 2011, **10**, 968.
22 Y. Liu, S. Zhou, Z. Zhuo, R. Li, Z. Chen, M. Hong and X. Chen, *Chem. Sci.*, 2016, **7**, 5013.
23 X. Liu, Z. Yi, X. Qin, H. Liu, W. Huang and X. Liu, *Adv. Opt. Mater.*, 2019, **7**, 1900519.
24 Q. Zhu, T. Sun, M. N. Chung, X. Sun, Y. Xiao, X. Qiao and F. Wang, *Dalton Trans.*, 2018, **47**, 8581.
25 X. Chen, L. Jin, T. Sun, W. Kong, S. F. Yu and F. Wang, *Small*, 2017, **13**, 1701479.
26 Q. Mei, A. Bansal, M. K. G. Jayakumar, Z. Zhang, J. Zhang, H. Huang, D. Yu, C. J. A. Ramachandra, D. J. Hausenloy, T. W. Soong and Y. Zhang, *Nat. Commun.*, 2019, **10**, 4416.
27 S. Wen, J. Zhou, K. Zheng, A. Bednarkiewicz, X. Liu and D. Jin, *Nat. Commun.*, 2018, **9**, 2415.
28 B. Chen and F. Wang, *Inorg. Chem. Front.*, 2020, **7**, 1067.
29 B. Chen, W. Kong, N. Wang, G. Zhu and F. Wang, *Chem. Mater.*, 2019, **31**, 4779.
30 J. C. Goldschmidt and S. Fischer, *Adv. Opt. Mater.*, 2015, **3**, 510.
31 S. Wilhelm, *ACS Nano*, 2017, **11**, 10644.
32 H. Dong, L. D. Sun and C. H. Yan, *Chem. Soc. Rev.*, 2015, **44**, 1608.
33 Y. I. Park, K. T. Lee, Y. D. Suh and T. Hyeon, *Chem. Soc. Rev.*, 2015, **44**, 1302.
34 D. Yang, P. Ma, Z. Hou, Z. Cheng, C. Li and J. Lin, *Chem. Soc. Rev.*, 2015, **44**, 1416.
35 X. Liu, X. Li, X. Qin, X. Xie, L. Huang and X. Liu, *Adv. Mater.*, 2017, **29**, 1702315.
36 J. Zhao, X. Chen, B. Chen, X. Luo, T. Sun, W. Zhang, C. Wang, J. Lin, D. Su, X. Qiao and F. Wang, *Adv. Func. Mater.*, 2019, **29**, 1903295.
37 D. Liu, X. Xu, Y. Du, X. Qin, Y. Zhang, C. Ma, S. Wen, W. Ren, E. M. Goldys, J. A. Piper, S. Dou, X. Liu and D. Jin, *Nat. Commun.*, 2016, **7**, 10254.
38 B. Xu, X. Zhang, W. Huang, Y. Yang, Y. Ma, Z. Gu, T. Zhai and Y. Zhao, *J. Mater. Chem. B*, 2016, **4**, 2776.
39 X. Chen, L. Jin, W. Kong, T. Sun, W. Zhang, X. Liu, J. Fan, S. F. Yu and F. Wang, *Nat. Commun.*, 2016, **7**, 10304.
40 B. Chen, Y. Liu, Y. Xiao, X. Chen, Y. Li, M. Li, X. Qiao, X. Fan and F. Wang, *J. Phys. Chem. Lett.*, 2016, **7**, 4916.

41 R. Shi, X. Ling, X. Li, L. Zhang, M. Lu, X. Xie, L. Huang and W. Huang, *Nanoscale*, 2017, **9**, 13739.
42 C. Ma, X. Xu, F. Wang, Z. Zhou, D. Liu, J. Zhao, M. Guan, C. I. Lang and D. Jin, *Nano Lett.*, 2017, **17**, 2858.
43 A. Pliss, T. Y. Ohulchanskyy, G. Chen, J. Damasco, C. E. Bass and P. N. Prasad, *ACS Photonics*, 2017, **4**, 806.
44 Y. Liu, X. Meng and W. Bu, *Coord. Chem. Rev.*, 2019, **379**, 82.
45 M. Wang, Y. Zhang, Q. Yao, M. Ng, M. Lin, X. Li, K. K. Bhakoo, A. Y. Chang, F. Rosei and F. Vetrone, *Chem. Mater.*, 2019, **31**, 5160.
46 T. Cheng, R. Marin, A. Skripka and F. Vetrone, *J. Am. Chem. Soc.*, 2018, **140**, 12890.
47 B. Ji, Y. E. Panfil, N. Waiskopf, S. Remennik, I. Popov and U. Banin, *Nat. Commun.*, 2019, **10**, 2.
48 A. Alinezhad, L. Gloag, T. M. Benedetti, S. Cheong, R. F. Webster, M. Roelsgaard, B. B. Iversen, W. Schuhmann, J. J. Gooding and R. D. Tilley, *J. Am. Chem. Soc.*, 2019, **141**, 16202.
49 R. B. Lewis, P. Corfdir, H. Küpers, T. Flissikowski, O. Brandt and L. Geelhaar, *Nano Lett.*, 2018, **18**, 2343.
50 R. W. Day, M. N. Mankin and C. M. Lieber, *Nano Lett.*, 2016, **16**, 2830.
51 C. Ratsch and A. Zangwill, *Surf. Sci.*, 1993, **293**, 123.
52 Y. Xiong, Y. Ma, J. Li, J. Huang, Y. Yan, H. Zhang, J. Wu and D. Yang, *Nanoscale*, 2017, **9**, 11077.
53 F. Wang, R. Deng and X. Liu, *Nat. Protoc.*, 2014, **9**, 1634.
54 S. G. Kwon, G. Krylova, P. J. Phillips, R. F. Klie, S. Chattopadhyay, T. Shibata, E. E. Bunel, Y. Liu, V. B. Prakapenka, B. Lee and E. V. Shevchenko, *Nat. Mater.*, 2015, **14**, 215.
55 R. C. Hibbeler, *Mechanics of Materials*, Pearson Prentice Hall, New Jersey, 2011.
56 M. Riaz, O. Nur, M. Willander and P. Klason, *Appl. Phys. Lett.*, 2008, **92**, 103118.
57 Y. He, X. Ren, Y. Xu, M. H. Engelhard, X. Li, J. Xiao, J. Liu, J.-G. Zhang, W. Xu and C. Wang, *Nat. Nanotechnol.*, 2019, **14**, 1042.
58 A. Nie, Y. Bu, P. Li, Y. Zhang, T. Jin, J. Liu, Z. Su, Y. Wang, J. He, Z. Liu, H. Wang, Y. Tian and W. Yang, *Nat. Commun.*, 2019, **10**, 5533.
59 P. Bhattacharya, R. Fornari and H. Kamimura, *Comprehensive Semiconductor Science and Technology*, Elsevier Science, New York, 2011.
60 A. Korkin, E. Gusev, J. K. Labanowski and S. Luryi, *Nanotechnology for electronic materials and devices*, Springer Science & Business Media, New York, 2010.
61 P. Sutter and M. Lagally, *Phys. Rev. Lett*., 2000, **84**, 4637.
62 J. B. Wachtman, W. E. Tefft, D. G. Lam and C. S. Apstein, *Phys. Rev.*, 1961, **122**, 1754.
63 B. Chen and F. Wang, *Trends Chem.*, 2020, **2**, 427.
64 Y. Fan, P. Wang, Y. Lu, R. Wang, L. Zhou, X. Zheng, X. Li, J. A. Piper and F. Zhang, *Nat. Nanotechnol.*, 2018, **13**, 941.
65 W. Kong, T. Sun, B. Chen, X. Chen, F. Ai, X. Zhu, M. Li, W. Zhang, G. Zhu and F. Wang, *Inorg. Chem.*, 2017, **56**, 872.
66 G. Pawley, *J. Appl. Crystallogr.*, 1981, **14**, 357.
67 M. Hÿtch, E. Snoeck and R. Kilaas, *Ultramicroscopy*, 1998, **74**, 131.
68 V. Grillo and F. Rossi, *Ultramicroscopy*, 2013, **125**, 112.
69 F. Sánchez-Bajo, F. Cumbrera, *J. Appl. Crystallogr.*, 1997, **30**, 427.